Control and Pointing Challenges of Antennas and Telescopes

Wodek Gawronski

Abstract— **Extremely large telescopes will be constructed in the near future, and new radiotelescopes will operate at significantly higher radio frequencies; both features create significantly increased pointing accuracy requirements that have to be addressed by control system engineers. The paper presents control and pointing problems encountered during design, testing, and operation of antennas, radiotelescopes, and optical telescopes. This collection of challenges informs of their current status, helps to evaluate their importance, and is a basis for discussion on the ways of improvement of antenna pointing accuracy.**

I. INTRODUCTION

In this paper we present pointing and control challenges that new antennas, radiotelescopes, and optical telescopes shall satisfy. Radiotelescopes perform operations at radiofrequencies lower than optical telescopes. They use parabolic dishes rather than mirrors. The dish size is larger (up to 100 meter) than mirrors of optical telescopes (up to10 m). Antennas are radiotelescopes that not only can receive radiofrequency signal, but also sent them. They are used for spacecraft communication. The newly designed antennas, radiotelescopes and telescopes have to satisfy control and pointing requirements that challenge existing technology. In order to increase the data rate, the antennas are required to communicate at higher radiofrequencies: from S-band (2.3 GHz), to X-band, (8.5 GHz), to Ka-band (32 GHz). The increased frequency requires more precise pointing: 28 mdeg for S-band, 8 mdeg for X-band, and 2 mdeg for Ka-band. The telescope size also increase, from 12 m Keck telescope to 30 or 50 m future telescopes now on drawing boards. The increased size creates multiple pointing and control challenges.

II. ANTENNA AND TELESCOPE EXAMPLES

A. NASA Deep Space Network

The NASA Deep Space Network (DSN) antennas communicate with spacecraft by sending commands (uplink) and by receiving information from spacecraft (downlink). To assure continuous tracking during Earth rotation the antennas are located at three sites: at Goldstone (California), Madrid (Spain), and Canberra (Australia). The signal frequencies are 8.5 GHz (X-band), and 32 GHz (Ka-band). The dish size of the antennas is either 34 meters or 70 meters. An example of the 70-meter antenna is shown in Fig.1. The antenna dish rotates with respect to horizontal (or elevation) axis. The whole antenna structure rotates on a circular track (azimuth track) with respect to the vertical (or azimuth) axis. For the Ka-band frequency the required tracking accuracy is on the order of 1 mdeg. This requirement is a driver for the control system upgrade of the antennas. In [1] and [2] one can find the description of the DSN antenna control systems, and at the webpage tmo.jpl.nasa.gov/tmo/progress_report/ the DSN antennas research reports, including control systems. The Deep Space Network webpage is at deepspace.jpl.nasa.gov/dsn/.

Figure 1. NASA/JPL 70-meter antenna at Goldstone, CA

Wodek Gawronski is with the Jet Propulsion Laboratory, California Institute of Technology, Pasadena, CA 91109, USA (e-mail: wodek.k.gawronski@jpl.nasa.gov)

B. *The Large Millimeter Telescope*

The Large Millimeter Telescope (LMT) project is the joint effort of the University of Massachusetts at Amherst and the Instituto Nacional de Astrofísica, Óptica, y Electrónica (INAOE) in Mexico. The LMT is a 50m diameter radio-telescope, designed for principal operation at wavelengths between 1mm and 4mm. The telescope is being built atop Sierra Negra (4640m), a volcanic peak in the state of Puebla, Mexico. The telescope construction expected to be complete in 2005. The LMT will be a significant step forward in antenna design: in order to reach its pointing accuracy specifications, it must outperform every other telescope in its frequency range. The antenna designer expects that the telescope will point to its specified accuracy of 1 arcsec under conditions of low winds and stable temperatures. More about LMT, see www.lmtgtm.org/.

C. *APEX Telescope*

The Max Planck Institute for Radioastronomy awarded a contract to Vertex Antennentechnik (Germany) to install the 12 m APEX (Atacama Pathfinder Experiment) telescope in the Chilean Atacama desert at Llano de Chajnantor at 5000 m altitude. This telescope will be used for observations in the sub-millimeter wavelength range. The overall surface accuracy of 20 microns and the pointing accuracy of 0.6 arcsec have been proven during acceptance testing which was carried out in 2004.

D. *ESA Deep Space Antennas*

For use in Deep Space, High Elliptical Orbit Missions, and future missions to Mars, the European Space Agency (ESA) procured 35 m Deep Space Ground Stations. The antennas are designed for frequencies up to 35 GHz and a pointing accuracy of 6 mdeg. The first antenna has been installed in Australia and has proven its compliance to the specifications. The second antenna is under construction in Spain. The 35 m antenna incorporates a full motion pedestal with a beam waveguide system.

E. *ALMA prototype*

It has been successfully installed and tested by Vertex. A brief description can be found at www.alma.nrao.edu/info. The pointing accuracy of the 12m ALMA telescope is 0.6 arcsec. The control system must handle very accurate movement at sidereal tracking velocities as well as several extremely fast switching functions. To do this, the drives are designed to accelerate up to 24 deg/s², which is very unusual for a telescope of this size.

F. *The Thirty Meter Telescope*

The Thirty Meter Telescope (TMT) will be the first of the giant optical/infrared ground-based telescopes addressing the compelling areas in astrophysics: the nature of Dark Matter and Dark Energy, the assembly of galaxies, the growth of structure in Universe, the physical processes involved in star and planet formation, and the characterization of extra-solar planets. TMT will operate over 0.3-30 μm wavelength range, providing 9 times the collecting area of the current largest optical telescope, the 10m Keck Telescope. It will use adaptive optics system to allow diffraction-limited performance, resulting in spatial resolution 12.5 times sharper than is achieved by the Hubble Space Telescope. More about TMT see at tmt.ucolick.org/.

G. *The Multiple Mirror Telescope*

The Multiple Mirror Telescope (MMT) is a joint project of the University of Arizona and the Smithsonian Institution. Located on Mount Hopkins, Arizona, the MMT is a 6.5m optical telescope used for spectroscopy, wide-field imaging, and adaptive optics astronomy.

Several advances in telescope design were pioneered at the MMT. Among these: Compact, altitude-azimuth structure with co-rotating building, in-situ aluminization of the primary mirror, and adaptive optics with deformable secondary mirrors and artificial guide stars.

The MMT was first designed as a multiple-mirror telescope, with six 1.8m primary mirrors in a single mount. Automated alignment of the individual light paths gave the telescope an equivalent aperture of 4.5m, with a 6.9m baseline for interferometry. The recent upgrade created a new 6.5m-class telescope, although significant challenges remain in improving the telescope performance in pointing and tracking, as the structural behavior of the new telescope is not completely understood and the control system is in the process of being re-designed. MMT webpage is www.mmto.org/ .

III. CONTROL SYSTEM STRUCTURE

A typical antenna is moved in azimuth (vertical) axis and elevation (horizontal) axis. The movements are independent, and their control systems are independent as well. Due to the independence, in the following we will consider a single axis only.

An antenna control systems consists of the rate and position feedback loops, as shown in Fig.2. The rate loop includes antenna structure and the drives. The drive (motor) rate is fed back to the rate controller. Typically, the rate loop is designed such that the antenna steady-state rate is proportional to the constant rate-loop input; the latter is called the rate command. The antenna position is measured with the azimuth and elevations encoders. The position loop is an outer loop that feds back the antenna position.

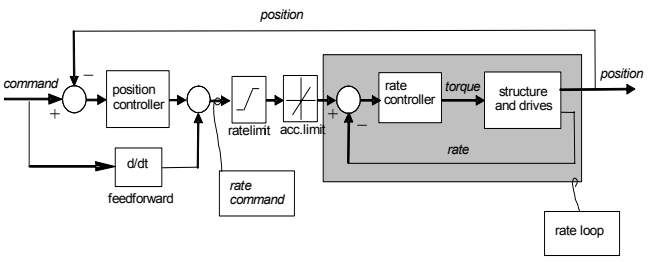

Figure 2. Antenna control system

The antenna rate and acceleration are limited (see Fig.2) and the limits reflect the restricted power of the antenna drives. During tracking the limits are not violated, however the rate and acceleration limits are hit during antenna slewing.

IV. CONTROL SYSTEM MODELS

Antenna control system models are indispensable in the antenna controller design and implementation stages for two reasons. In the design stage, they are used to determine the controller gains and to asses the control system performance; in the implementation stage the models are part of antenna controllers, and help to fine-tune the antenna pointing precision.

In the design stage an analytical model of the control system is developed. It includes the finite element model of a structure, motor and gearbox models, amplifiers and filters, and also nonlinearities: friction, backlash, rate and acceleration limits. An example of such model is given in [3] and [4]; drive system model in [5] and [6].

In the implementation stage the antenna model is obtained from the open-loop antenna field tests, using a system identification procedure. The model accuracy is particularly important when the antenna controller is a model-based controller, such as LQG or H_∞ controller.

In order to obtain the model an antenna is excited with the white noise (a noise is "white", if its bandwidth is much wider than the bandwidth of the open-loop antenna), and the encoder output is recorded. From the input and output records the transfer function is obtained [7], [1] and the example of the azimuth transfer function of the 34-meter antenna is shown in Fig.3, dashed line. From the input-output data the system state-space model is identified. In Fig.3 the magnitude of the transfer function obtained from the identified state-space model is shown in solid line. The magnitude of the transfer function consists of the rigid body part that dominates lower frequencies (below 1 Hz), and is characterized with the -20 dB/dec slope. At higher frequencies – above 1 Hz – the transfer function shows flexible deformations characterized by resonant peaks. The development of the control system based on the identified model one can find in [8] and [1]; on a telescope identification using swept-sine generator, see [9]; on Gallileo Telescope model identification see [10].

The antenna azimuth model depends on the antenna elevation position. Note, for example, that an antenna with its dish at zenith has different structural properties than the antenna with its dish pointed horizontally. Figure 4 shows the measured magnitudes of the azimuth transfer functions for a 34-meter antenna at different elevation positions. The variations of the first two natural frequencies with respect to the antenna elevation position are shown in Fig.5. From these figures we see that the natural frequencies depend on the antenna elevation position: the second frequency changes significantly with the elevation angle.

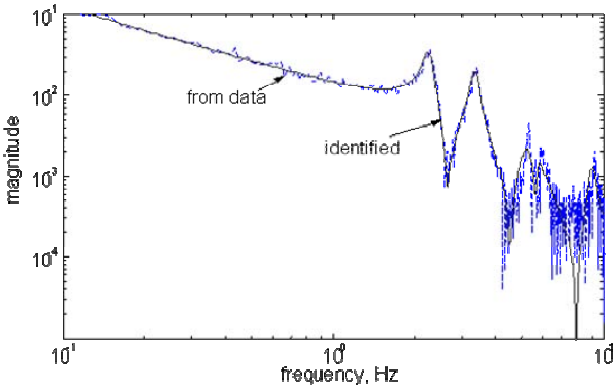

Figure 3. Magnitude of the transfer function of 34-meter DSN antenna

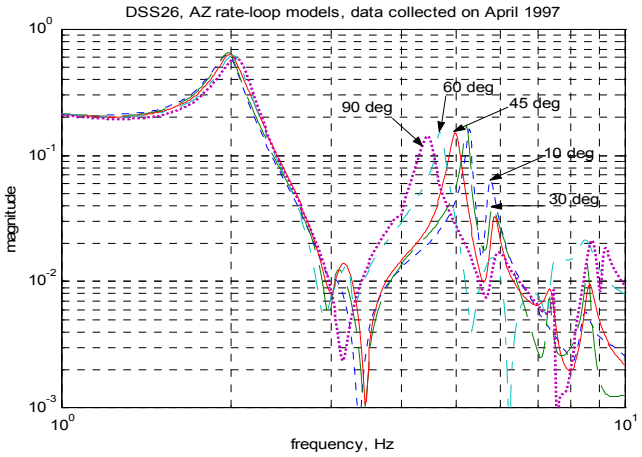

Figure 4. Magnitude of the azimuth transfer function of 34-meter DSN antenna for different elevation angles

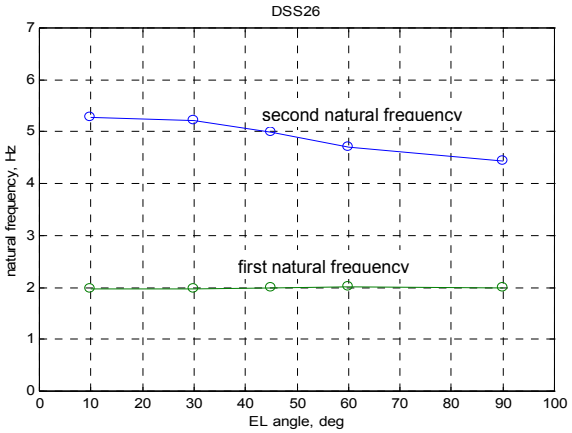

Figure 5. The variation of the two first natural frequencies of the antenna structure as a function of its elevation position.

Antenna natural frequencies depend also on the antenna size. It is a general tendency that the natural frequencies decrease with the increase of the antenna size (the structure becomes "softer"). The lowest natural frequency (called the fundamental frequency) is considered a measure of compliance of the structure. The Aerospace Corporation collected data of fundamental frequencies of many antenna structures. In these data the decreasing

tendency of frequencies with the increase of antenna dish size is observed. Based on these data, we determined the best-fit line (in logarithmic scale) defined by the following equation

$$f = 20.0\, d^{-0.7} \tag{1}$$

The line is presented in Fig.6. In the above equation d is antenna diameter in meters, and f is the antenna fundamental (lowest) frequency in Hz. This equation represents the average natural frequency for a given antenna diameter. Equation (1) allows evaluating the structural soundness of a particular antenna: if the fundamental frequency of the considered antenna structure is higher than the frequency obtained from Eq. (1), the structure is stiffer than the average (thus of better pointing performance), if it is lower – the structure is softer than average (thus of inferior pointing performance).

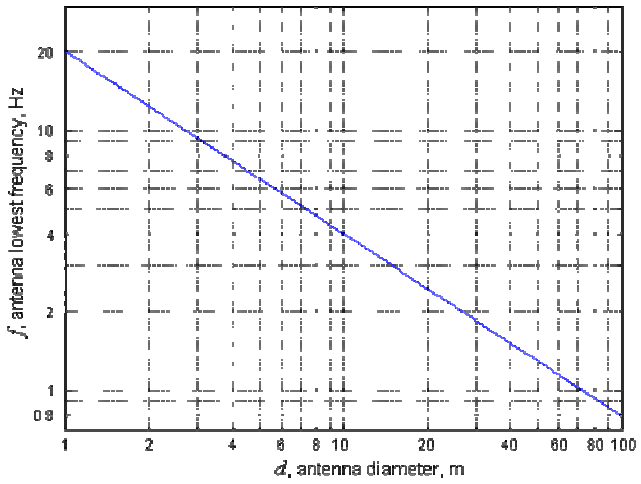

Figure 6. The best-fit line that fits the Aerospace Corp. chart of antenna fundamental frequencies.

V. DISTURBANCE MODEL

The antenna main disturbance is wind. Wind gusts spectra depend on the geographical location and on terrain profile. Different spectra, based on wind gusts measurements, are used to model wind gusts. We present here the Davenport spectrum, $S_v(\omega)$, that depends on average wind speed and terrain roughness as follows [11]

$$S_v(\omega) = 4800 v_m \kappa \frac{\beta\omega}{(1+\beta^2\omega^2)^{4/3}} \tag{2}$$

where v_m is the mean wind speed, β=600/πv_m, and κ is the surface drag coefficient, obtained from the roughness of the terrain, see [12] $\kappa = \left(2.5\ln(z/z_o)\right)^{-2}$. In the above equation z is the distance from the ground to the antenna dish center, and z_o is the height of the terrain roughness (e.g., z_o= 0.1 to 0.3 m at Goldstone, CA). For 34-meter antennas z=17 m, thus κ=0.006 to 0.010. The Davenport spectrum is shown in Fig.7, solid line.

In order to model wind gusts in time domain, the spectrum is approximated with a linear filter. The filter was obtained in [13], by adjusting the filter parameters, such that the magnitude of the filter transfer function best fits the Davenport spectrum within the antenna bandwidth of [0.001, 20] Hz. The resulting digital filter transfer function is for the sampling time of 0.02 s is as follows

$$G_w = \frac{0.1584z^3 - 0.3765z^2 + 0.2716z - 0.0534}{z^4 - 2.9951z^3 + 3.0893z^2 - 1.1930z + 0.0988} \tag{3}$$

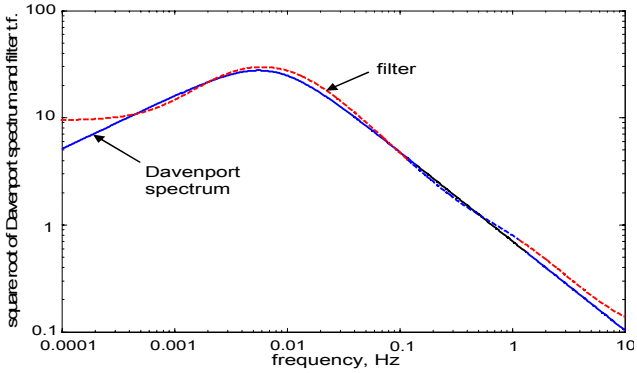

Figure 7. The Davenport spectrum and its approximating filter.

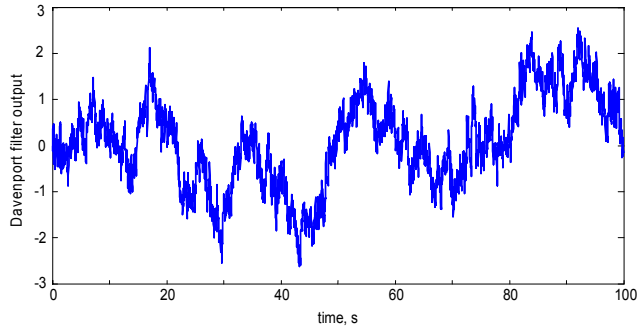

Figure 8. The wind gust time history obtained from the Davenport filter.

The plot of the magnitude of the filter transfer function is shown in Fig.7. A sample of the wind speed generated by the filter is shown in Fig.8.

Having wind speed, the wind force is obtained (in Newtons) as follows:

$$F_w(t) = k_f \Delta v(t) \tag{4}$$

where $k_f = 0.000892 v_m^2$, and v_m is the wind mean speed, m/s, see [14]. On Gemini Telescope wind model see [15], and on steady-state wind modeling see [16], on wind simulations see [17].

VI. POSITION CONTROLLERS

We present an antenna performance with PI, LQG, and H_∞ position controllers. On the application of predictive controller to antenna control, see [18]; on periodic disturbance rejection see [19].

A. Antenna performance with PI controller

Consider the proportional (P) and integral (I) actions independently. Assuming a zero integral gain, k_i=0, and the proportional gain k_p=0.5 the response of the closed loop system to a 10-mdeg step command is shown in Fig.9a. It has no overshoot and a settling time 7s. The response to 10 mdeg/s rate offset has constant servo error (or lagging) of 20 mdeg, see Fig.9b. The lag can be reduced by increasing the proportional gain. Indeed, increasing the gain to 1.6 produces 6 mdeg lag; note, however, that the system is almost unstable (see the step response in Fig.9a). Thus, the proportional controller cannot completely eliminate the lagging.

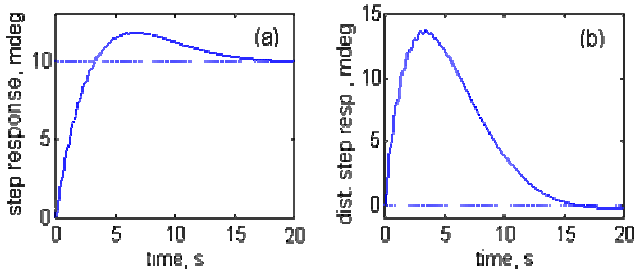

Figure 9. Antenna performance with the PI controller

The integral gain eliminates the lagging. A simulation the antenna response to the 10 mdeg/s rate offset (with proportional gain k_p=0.5 and integral gain, k_i=0.1) is shown in Fig.10. Indeed, the rate-offset response has zero steady-state error, as a result of the action of the integrator (for non-zero steady-state error the integral of the error grows indefinitely causing strong controller action). On the other hand, the integrator of the PI controller produces an overshoot, see Fig.9a.

The response of the PI controller to 10 mdeg/s disturbance step (pictured in Fig.9b) is slow and of large amplitude. The servo error in 10 m/s wind gusts is quite large: 5.8 arcsec, see Table 1. The variable structure PI controller was described in [20].

TABLE 1
RMS SERVO ERROR IN 10 M/S WIND GUSTS

Controller	AZ servo error (arcsec)	EL servo error (arcsec)
PI	1.8 #	5.8#
LQG	0.10	0.39
H_∞	0.08	0.18

from measurements, see [21].

B. Antenna performance with feedforward controller

The feedforward loop is added to improve its tracking accuracy at high rates [2]. In this loop the command is differentiated and forwarded to the rate-loop input, see Fig.2. The derivative is an approximate inversion the rate loop transfer function. In this way we obtain the open-loop transfer function from the command to the encoder approximately equal to 1. Indeed, the magnitude of the rate-loop transfer function G_r is shown in Fig.11. It is approximated (up to 1 Hz) with an integrator ($G_{rapprox} = 1/s$), shown in the same figure, dashed line. The feedforward transfer function is a derivative ($G_{ff} = s$) shown in Fig.11, dash-dotted line, so that the overall open-loop transfer function is a series of the feedforward and the rate loop $G_o = G_r G_{ff}$, which is approximately equal to 1 up to the frequency 1 Hz. The position feedback is added to compensate disturbances and system imperfections.

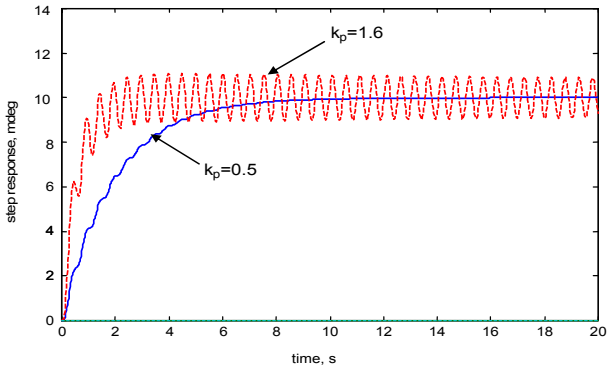

Figure 10. Limits of performance of the PI controller

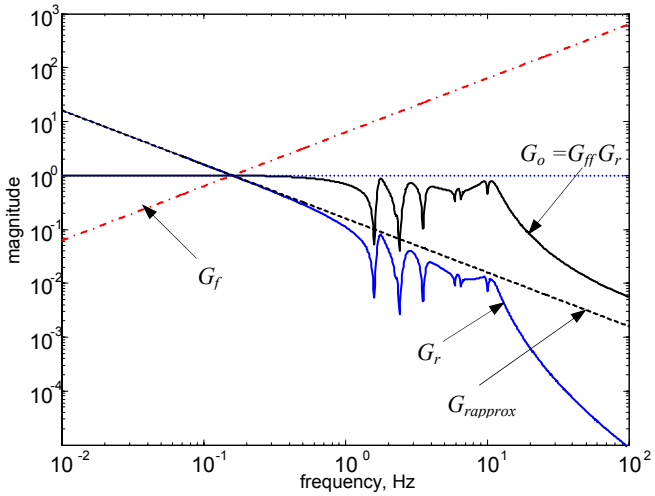

Figure 11. The feedforward action is illustrated with the magnitudes of the transfer functions (G_r is the rate-loop transfer function, $G_{rapprox}$ is the rate-loop transfer function approximation, G_{ff} is the feedforward loop transfer function, and $G_o = G_{ff} G_r$ is the transfer function of the series connection of feedforward and rate-loops).

C. Antenna performance with LQG controller

It has been noted that the bandwidth, the speed of the system response, and the disturbance suppression abilities of the PI controller improve with the increase of the

controller proportional gain (up to a limiting value at which the antenna vibrates). If the vibrations could be sensed and controlled the performance could be further improved. Encoder is the antenna position sensor. The Fourier transformation of the encoder measurements shows antenna vibrations, indicating that the antenna vibrations can be recovered from the encoder data. This can be done using an estimator, as in Fig.12. The estimator is an analytical antenna model driven by the same input as the antenna itself, and by the estimation error (the difference between the actual encoder reading and the estimated encoder reading). The error is amplified with the estimator gain k_e to correct for transient dynamics, Fig.12. The estimator returns the antenna states that consists of the estimated encoder reading (or noise free encoder measurements), and the estimated states x_f of the flexible deformations of the antenna structure. The latter states effectively replace the missing vibration measurements. The resulting controller's output is a combination of the PI controller outputs and the flexible mode controller output. The first take care of the tracking motion, the latter suppresses the antenna vibrations. In the above configuration the increased proportional and integral gains do not destabilize the closed-loop system, since the flexible-mode controller keeps the antenna vibrations suppressed. If the gain determination procedure minimizes the so called LQG index the controller is called an LQG controller. The description of the LQG controller design one can find in [1] and [7], and a design tool is described in [22]. The application of the LQG controller to 20m radiotelescope is described in [23].

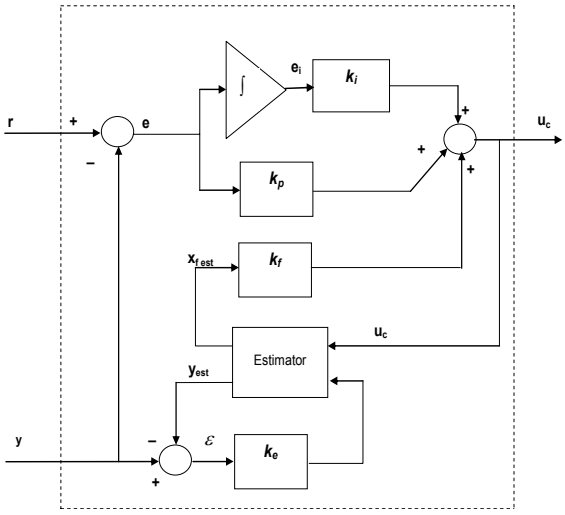

Figure 12. The LQG controller structure

The performance of the LQG controller designed for a 34-meter antenna is illustrated in Fig.13a (the response to a 10 mdeg step command), and in Fig.13b (the response to 10 mdeg/s disturbance step). The step response has small settling time of 2 s, and disturbance step response has low magnitude of short duration (2 s). The rate offset shows zero lagging. The servo error in 10 m/s wind gusts is small: 0.10 arcsec (Table 1). These parameters show that the LQG controller is of an order better than the PI controller.

D. Antenna performance with H_∞ controller

H_∞ controllers outperform LQG controllers in many applications. The structure of an H_∞ controller is similar to that of the LQG controller, but its parameters are obtained from a different algorithm. While LQG controller minimizes the system H_2 norm (its rms response to the white noise input), the H_∞ controller algorithm minimizes the system H_∞ norm (in case of single-input-single-output system, the system H_∞ norm is the maximal magnitude of its transfer function).

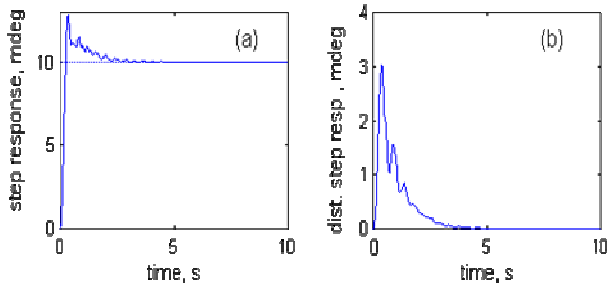

Figure 13. Antenna performance with LQG controller

The antenna H_∞ controller was designed by shaping the disturbance input. A filter of the Davenport wind spectrum profile was used as a shaping (or weighting) factor. The H_∞ controller design for antenna tracking purposes is described in [1] and [24]. The performance of the antenna is shown in Fig.14. The figures show very small settling time (1.2 s), small overshoot (less than 10%). These features significantly exceed LQG controller performance. The response to the 10 mdeg/s rate offset has zero steady-state error. The servo error in 10 m/s wind gusts is small: 0.08 arcsec, see Table 1. The application of the H_∞ controller to the airborne telescope SOFIA is described in [25], for Thirty Meter Telescope in [26], to a segmented mirror telescope in [27] and [28], and to the secondary mirror of a Giant Segmented Mirror Telescope in [29].

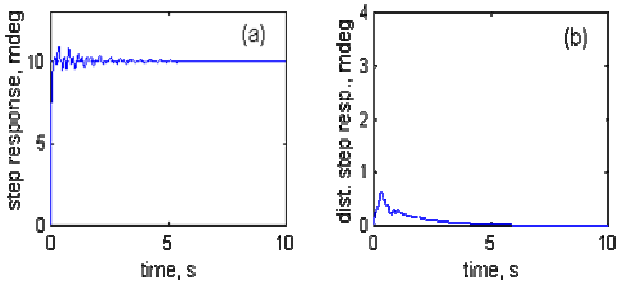

Figure 14. Antenna performance with H_∞ controller

VII. COMMAND PREPROCESSOR

When LQG or H_∞ controller is implemented, it initiates limit cycling during antenna slewing operations. This phenomenon is caused by the antenna rate and acceleration limits: the controllers are designed for a linear plant, while limits cause antenna non-linear dynamics. In order to avoid the cycling one can either apply different controllers for tracking purposes, and for slewing; or implement an anti-windup technique, see [30]; or apply a controller with variable gains [20], [31]; or use a trajectory calculated in advance, such that it never exceeds the rate and acceleration limits [32]; or use a command preprocessor (CPP). This paper presents the latter approach. The preprocessor is a computer program that generates a modified command, identical with the original one, if the rate and accelerations are within the limits; and a command of maximal (or minimal) rate and acceleration, when the limits are met or violated. The location of the preprocessor in the antenna control system is shown in Fig.15.

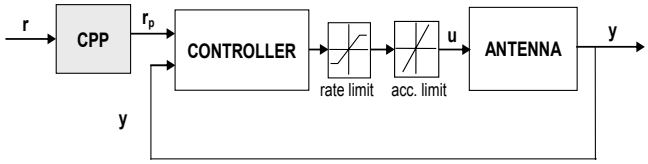

Figure 15. The CPP location in the antenna control system

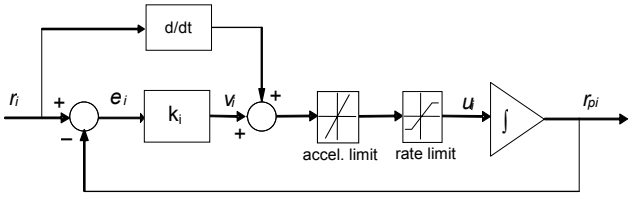

Figure 16. The CPP block diagram.

The block diagram of the CPP is shown in Fig.16. It imitates a rigid antenna (represented by the integrator) driven by variable-gain controller with a feedforward gain (the latter represented by the derivative). The variable gain k_i depends on the preprocessor error e_i as follows

$$k_i = k_o + k_v e^{-\beta|e_i|} \tag{5}$$

In this equation k_o is the constant part of the gain, k_v is the variable part of the gain, and β is the error exponential. The plot of $k_i(e_i)$ for k_o=1, k_v=5, and β=20 is shown in Fig.17. The detail description of CPP is given in [12].

The CPP response to the step of 10 deg is shown in Fig.18. Preprocessed command begins with the maximal acceleration until it reaches the maximum rate, then continues with the maximal (and constant) rate and finally slows-down with the minimal deceleration. After reaching the value of 10 deg the error between the original and the preprocessed command is zero.

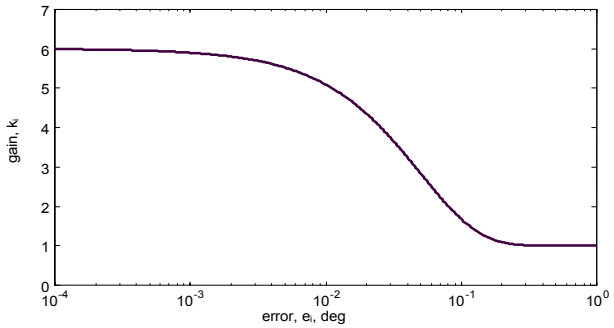

Figure 17. The CPP gain versus CPP error.

The measured responses of the antenna to a large (non-processed) step input of 10 deg are shown in Fig.19a. Clearly, an unstable limit cycling is present. The same response of the antenna with processed command is shown in Fig.19b, where the antenna follows closely the processed command, without limit-cycling.

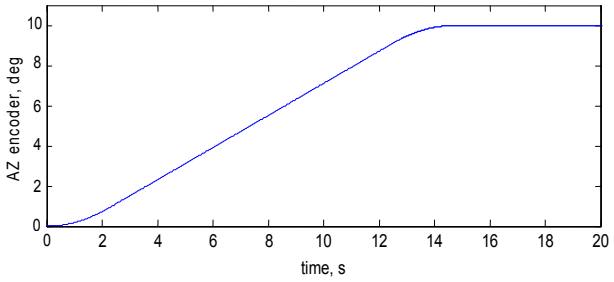

Figure 18. The CPP response to 10-deg step

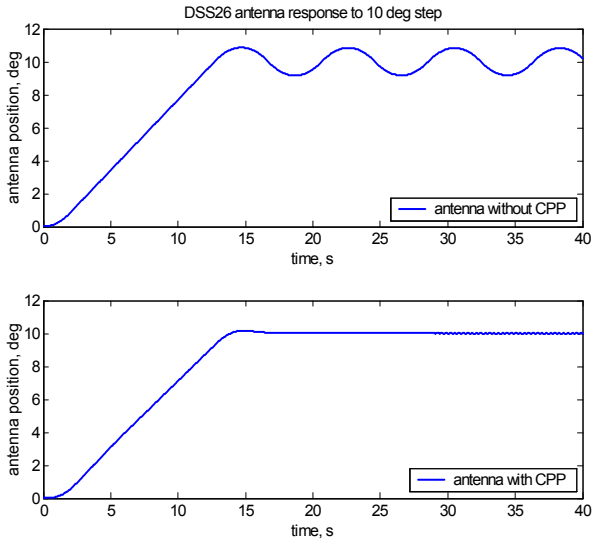

Figure 19. Antenna response to 10 deg step: (a) without CPP, and (b) with CPP.

VIII. POINTING ERROR SOURCES

The following is a list of the main pointing error sources that are not detectable by the antenna sensors encoders):

- The antenna encoders are not collocated with the RF beam, thus the beam position is measured with a certain bias.
- The antenna control torques are applied at the motor locations, while the wind disturbances are distributed over the antenna surface; thus only certain portion of the disturbances can be compensated with the motors..
- Disturbances. Thermal, and wind forces are the main sources of disturbances and are difficult to measure. Gravity forces, and azimuth track imperfections are measurable and repeatable disturbances. Atmospheric refraction is a measurable but unrepeatable disturbance.
- Model uncertainty. Manufacturing imperfections and the variable antenna configuration (its structural properties depend on its elevation angle) are the sources of uncertainty that limit the controller performance.
- Nonlinearities. Backlash and friction torques at the antenna drives, rate and acceleration limits are the main sources of nonlinearity.

The pointing error sources and corrections for the Green Bank telescope are presented in [33]; for active corrections of structural deformations see [34]; for tracking performance [35]; on use of inclinometers for measuring telescope position see [36]; on thermal and wind control of the Very Large Telescope (European Southern Observatory) see [37].

A. Azimuth track imperfections

Antenna rotates in azimuth on a circular azimuth track, which is manufactured with level precision of ±0.5 mm for the 34-m DSN antennas. The uneven azimuth track level causes antenna tilts and flexible deformations. The finite element model of the alidade (lower antenna structure) deformations due to track unevenness is shown in Fig.20. Certainly, these deformations impact antenna pointing accuracy. However, the pointing errors caused by the track irregularities are repeatable therefore they can be calibrated. By developing a look-up table one provides pointing corrections as a function of the antenna azimuth position. The look-up table is generated by using inclinometers that measured tilts of the alidade structure at selected points.

Four inclinometers were installed on the alidade structure, at locations marked in Fig.21. Each inclinometer measures tilts of its *x*- and *y*-axes. The locations of the inclinometers were selected such that their tilts estimate the alidade elevation and cross-elevation rotations at the antenna focal point. Inclinometers No.1 and 2 are located at the top of the alidade. Inclinometer No.2 is located next to the elevation encoder. The *y*-axis tilt of this inclinometer reflects the elevation pointing error. Inclinometers No 3 and 4 are located in the middle of the crossbeam of the left and right sides of the alidade, respectively. Their *x*-axis tilts combined with the *x*-axis tilts of the inclinometers No.1 and 2, give the cross-elevation pointing error, as shown below.

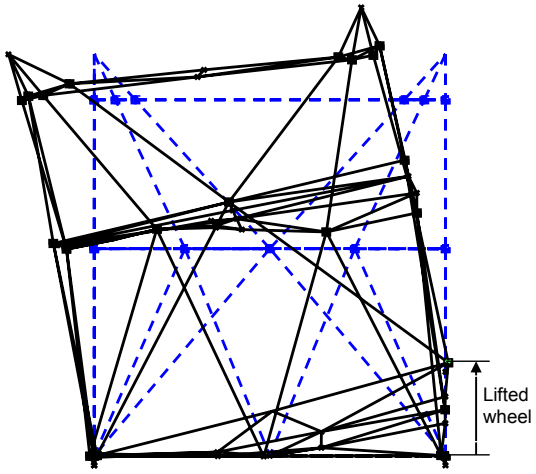

Figure 20. Alidade deformation due to wheel lift.

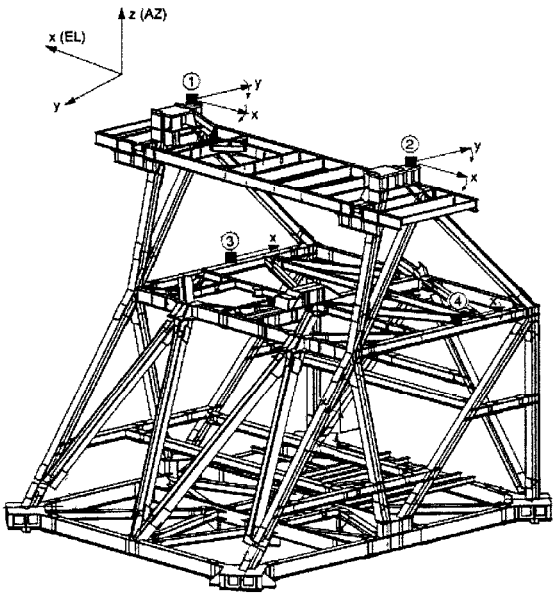

Figure 21. Alidade and the inclinometer locations.

The *x*- and *y*-axis tilts of the *i*th inclinometer are denoted α_{ix} and α_{iy}, respectively. The inclinometer data were collected during the antenna azimuth rotation at constant rate of 50 mdeg/s, and the sampling frequency of 2 Hz. The tests were performed during nighttime to minimize deformations of the antenna structure due to the thermal gradient. The data show satisfactory repeatability.

The antenna elevation error Δ_{el} is the *y*-tilt of the second inclinometer

$$\Delta_{el} = \alpha_{2y} \tag{6}$$

The cross-elevation error (Δ_{xel}) depends on the antenna elevation position (θ), and on the rotation (δ_y) of the top of the alidade with respect to the y-axis (tilt of the elevation axis) and the alidade twist δ_z (the rotation of the top of the alidade with respect to the z-axis):

$$\Delta_{xel} = \delta_z \cos(\theta) - \delta_y \sin(\theta) \quad (7)$$

The tilt of the elevation axis is an average of the x-tilts of the inclinometers 1 and 2, that is,

$$\delta_y = 0.5(\alpha_{1x} + \alpha_{2x}) \quad (8)$$

while the alidade twist is determined from x-tilts of the inclinometer No3 and No4,

$$\delta_z = \frac{h}{l}(\alpha_{7x} - \alpha_{8x}) \quad (9)$$

where h is the alidade height, and l is the distance between the inclinometers. The details are in [38].

The reading of the inclinometer 1, x-axis, is shown in Fig.22. The fitted sinusoid shows the azimuth axis tilt. The pointing error obtained from the inclinometer measurements is shown in Fig.23, dashed line. The measurements of the actual pointing error (using conscan technique) are shown in the same figure, solid line with dots. The figure shows the coincidence of the inclinometer and conscan data.

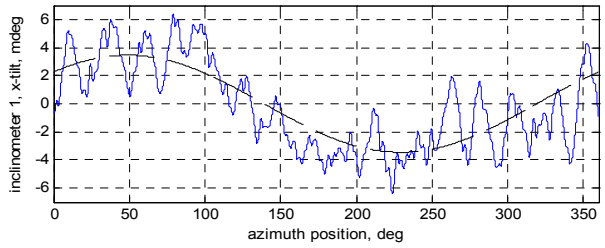

Figure 22. Inclinometer No.1 tilt, x-direction.

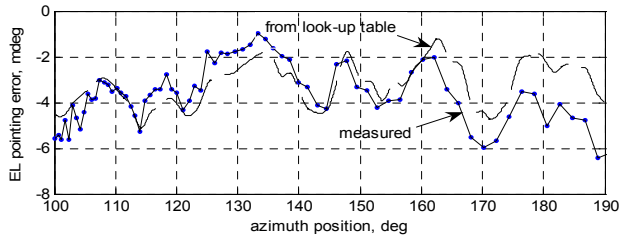

Figure 23. Antenna elevation pointing error due to track level unevenness: from the look-up table (dashed line), and measured by conscan (solid line with dots)

B. Thermal deformations.

The temperature gradient causes deformations of the antenna structure, thus it impacts the pointing accuracy. The inclinometers were used to measure antenna tilts when it was stowed. A sample shown in Fig.24 shows tilts of 8 mdeg. The largest tilts were in afternoons, when the sun heat was intensive (although the data were collected in November, which is not the hottest day at the Mojave Desert, where antennas are located). On techniques to compensate for the thermal deformations see [39], [37], and [40].

C. Gravity deformations

Gravity forces deform antenna dish and subreflector, and the deformations depend on the dish elevation position. These deformations are repeatable and can be calculated comparatively accurately using the finite element model. The gravity deformations of the 70-meter antenna are shown in Fig.25. The calculated deformations allow to generate a look-up table of the pointing corrections.

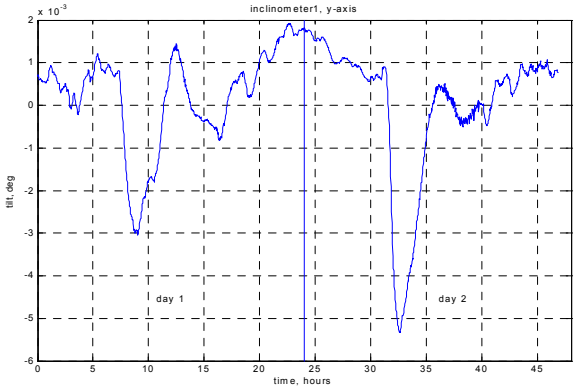

Figure 24. Thermal deformations of the 34-meter DSN antenna.

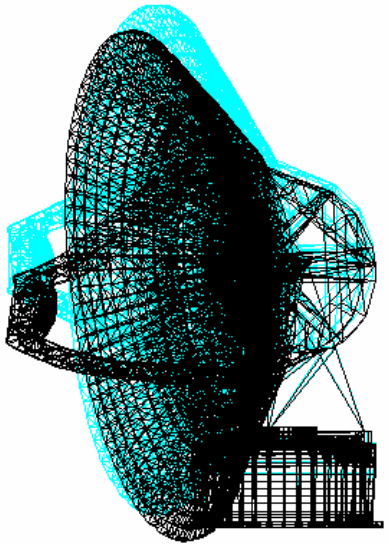

Figure 25. Gravity deformation of the 70-meter antenna

D. Atmospheric refraction

The RF beam is bent while passing through the atmosphere, see Fig.26. The amount of refraction depends on air humidity, and can be calculated. The atmospheric conditions are monitored by weather stations, and refraction model calculates the correction once a second. The refraction corrections are added to the antenna pointing

model, and they can be of order of several hundred milidegrees.

E. Friction

Antenna/telescope drive friction can cause pointing errors. In order to improve pointing, the best thing is to reduce the friction. For example the 70-meter DSN antennas use oil film to rotate in azimuth. Machine jack-screws, often used in elevation drives, are sources of significant friction. When friction cannot be reduced through structural modifications a control engineering tools are implemented. One of them is dither, i.e., oscillations applied at the friction source to break the friction contact. The dither frequency shall be higher than the antenna structural frequencies, to avoid excitation of structural resonances. The analysis of dither as applied to the antenna is given in [41]. The friction modeling of the 2.5 meter telescope is described in [42]; more on friction compensation, see [43], [44], and [45].

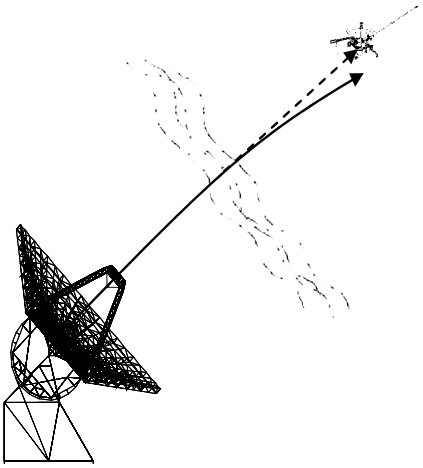

Figure 26. Atmospheric refraction

F. Backlash

Gearboxes and gears are an antenna drive components. A backlash phenomenon at the gearboxes is observed when one gear rotates through a small angle without causing a corresponding movement of the second gear. This causes beating in the drives, gear wear, and deterioration of antenna tracking precision. In order to maintain antenna pointing precision the backlash phenomenon is eliminated by implementing two symmetric drives with a specific torque difference between them, see Fig.27. The torque difference is called a torque bias, or counter-torque. With two motor configurations the backlash clearance will occur at one drive while the other is still coupled. The antenna dynamics will be controlled by the latter drive. The effectiveness of the two-motor approach depends on the amount of torque bias applied at the drives, which depends on the antenna variable load. The torque bias should be large enough to lead the antenna through the gap for the maximal allowable torque load, but small enough that it will not cause excessive local stress, friction, or wear. More on backlash, see [46], [47], [48], [49], [50], [51], [52] and [53].

IX. POINTING ERROR CORRECTION

A. Look-up tables

They are used to correct for the known and repeatable errors (e.g. gravity deformations, azimuth track level corrections). For non-repeatable errors an additional feedback (e.g., conscan or monopulse) is applied.

B. Conical scan (conscan)

Conscan is an additional feedback. This technique is commonly used for the determination of the true spacecraft position. During conscan, circular movements are added to the antenna command as shown in Figure 28. The circular movements cause sinusoidal variations of the power of the signal received from the spacecraft, as illustrated in Fig.29. The power variations are used to estimate the true spacecraft position. The time of one cycle is between 30 and 60 s, thus the correction update is comparatively slow. The drawback of this technique is that antenna is always off the peak power, i.e., always slightly off the target.

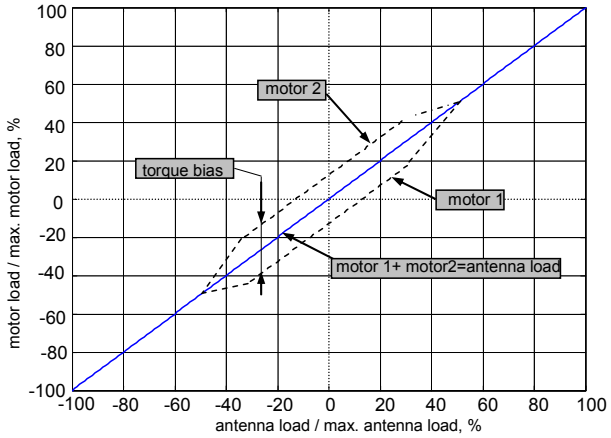

Figure 27. Motor torques and the counter-torque.

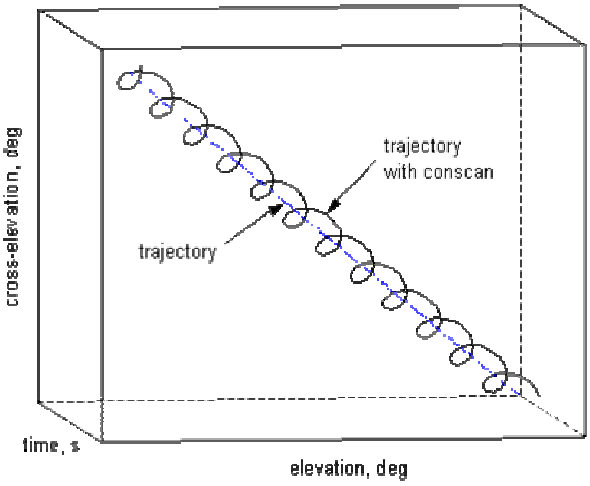

Figure 28. Antenna trajectory when performing conical scan.

The control system of the conscan consists of the additional (outer) feedback that corrects for the difference between encoder and RF beam position, see Fig.30. More about conscan, see [54] and [55].

C. Monopulse

In this algorithm the pointing error is estimated from RF signals received by the monopulse feed-horn. These signals are uniquely related in amplitude and phase as a function of the antenna pointing error. The single monopulse feed design allows direct pointing at the target at all times, allowing for the spacecraft to be tracked at the peak of the antenna pattern. This technique is much faster than conscan (updating time is 0.02 s). More about monopulse see [56] and [57].

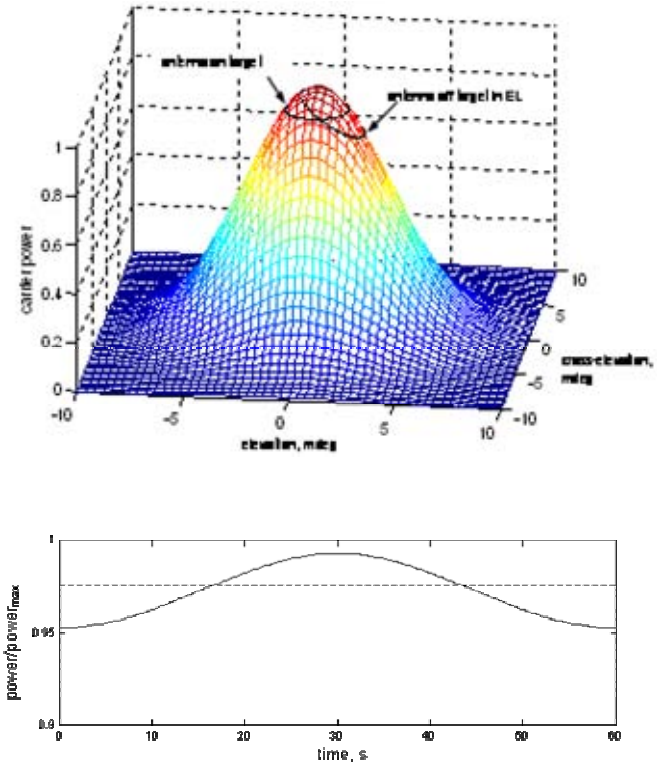

Figure 29. Antenna power variation during conscan.

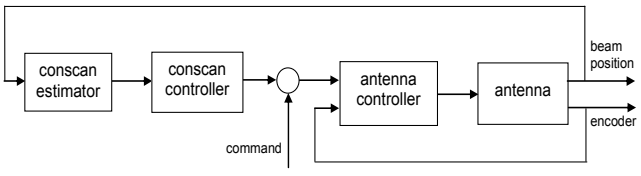

Figure 30. Antenna conscan controller.

X. CONCLUSIONS

The paper presents the challenges that control system engineers encounter while trying to satisfy the demanding pointing requirements. Not all challenges have satisfactory solutions. One of the reasons is the lack of a stable point of reference to measure the RF beam position. The substitute beam position measurements using encoders are subject to painstaking corrections, which not always satisfy the requirements. A fast and inexpensive measurement system of beam position would be a breakthrough in the antenna/telescope technology.

ACKNOWLEDGMENT

A portion of the research described in this paper was carried out by the Jet Propulsion Laboratory, California Institute of Technology, under a contract with the National Aeronautics and Space Administration.

REFERENCES

[1] Gawronski, W., *Advanced Structural Dynamics, and Active Control of Structures,* Springer, New York, 2004.

[2] W. Gawronski, and J.A. Mellstrom, "Control and Dynamics of the Deep Space Network Antennas," a chapter in *Control and Dynamic Systems*, vol.63, ed. C.T. Leondes, Academic Press, San Diego, 1994.

[3] W. Gawronski and K. Souccar, "Control system of the Large Millimeter Telescope," *SPIE Astronomical Telescopes and Instrumentation Conference*, Glasgow, June 2004.

[4] D. Clark "Control system prototyping – A case study" Technical Memo, ITM-04-3, www.mmto.org/MMTpapers/tech00_10.shtml#2004

[5] T. Erm and P. Gutierrez, "Integration and tuning of the VLT drive systems," *Proc. SPIE Telescope Structures, Enclosures, Controls, Assembly/Integration/Validation and Commissioning,* Vol.4004, 2000.

[6] S. Jimenez-Garcia, M.E. Magana, J.S. Benitez-Read, and J. Martinez-Carbalido, "Modeling, simulation, and gain scheduling control of large radiotelescopes," *Simulation Practice and Theory*, vol. 8, pp.141-160, 2000.

[7] W. Gawronski, C. Racho, and J. Mellstrom, "Application of the LQG and feedforward controllers for the DSN antennas," *IEEE Trans. on Control Systems Technology*, vol.3, 1995, also see tmo.jpl.nasa.gov/tmo/progress_report/42-109/109R.PDF, tmo.jpl.nasa.gov/tmo/progress_report/42-112/112J.PDF.

[8] W. Gawronski, H. G. Ahlstrom, and A. M. Bernardo, "Analysis and performance of the control systems of the NASA 70-meter antennas," *ISA Transactions,* 2004, also see tmo.jpl.nasa.gov/tmo/progress_report/42-144/144D.pdf

[9] D. Clark, "Selected results of recent MMT servo testing," Technical Memo, ITM-03-5, www.mmto.org/MMTpapers/pdfs/itm/itm03-5.pdf

[10] E. Cascone, D. Mancini, and P. Schipani, "Galileo Telescope model identification," *Proc. SPIE,* vol. 3112, pp.343-350, 1997.

[11] E. Simiu and R.H. Scanlan, *Wind Effects on Structures,* Wiley, New York 1978.

[12] W. Gawronski, W. Almassy, "Command pre-processor for radiotelescopes and microwave antennas," *IEEE Antennas and Propagation Magazine*, vol.44, No2, 2002, also see htmo.jpl.nasa.gov/tmo/progress_report/42-136/136A.pdf ipnpr.jpl.nasa.gov/tmo/progress_report/42-150/150G.pdf

[13] W. Gawronski, B. Bienkiewicz, and R.E. Hill, "Wind-induced dynamics of a Deep Space Network antenna," *Journal of Sound and Vibration*, vol.178, No.1, 1994, also see tmo.jpl.nasa.gov/tmo/progress_report/42-108/108J.PDF

[14] W. Gawronski, "Modeling Wind Gusts Disturbances for the Analysis of Antenna Pointing Accuracy," *IEEE Antennas and Propagation Magazine*, vol.46, 2004, also see ipnpr.jpl.nasa.gov/tmo/progress_report/42-149/149A.pdf

[15] G.Z. Angeli, M.K. Cho, M. Sheehan, and L.M. Stepp, "Characterization of Wind Loading of Telescopes," *Proc. SPIE, Integrated Modelingvof Telescopes,*vol. 4757, pp.72-83, 2002.

[16] W. Gawronski, J. Mellstrom and B. Bienkiewicz, "Antenna Mean Wind Torques: A Comparison of Field and Wind Tunnel Data," *IEEE Antennas and Propagation Magazine*, 2004.

[17] J. Mann, "Wind field simulations, *Prob. Engrg. Mech.,* vol. 13, pp. 269-282, 1998.

[18] W. Gawronski, "Predictive controller and estimator for NASA Deep Space Network antennas," *ASME Transactions, Journal of Dynamic Systems, Measurements, and Control*, No2, 1994, also see tmo.jpl.nasa.gov/tmo/progress_report/42-104/104D.PDF.

[19] T. Erm, and S. Sandrock, "Adaptive periodic error correction for the VLT telescopes," *Proc. SPIE Large Ground-Based Telescopes*, Vol. 4837-106, 2002

[20] D. Mancini, M. Brescia, E. Cascote, P. Schipani, "A variable structure control law for telescopes pointing and tracking," *Proc. SPIE,* vol.3086, 1997.

[21] W. Gawronski, "Antenna control systems: from PI to H_∞," *IEEE Antennas and Propagation Magazine*, vol.43, no.1, 2001

[22] Maneri, E., and W. Gawronski, "LQG controller design using GUI: application to antennas and radio-telescopes," *ISA Transactions,* 2000, also tmo.jpl.nasa.gov/tmo/progress_report/42-140/140D.pdf

[23] M. Olberg, C. Lindeborg, A. Seyf, and C.F. Kastengren, "A simple robust digital controller for the Onsala 20m radio telescope," *Proc. SPIE,* vol. 2479, pp.257-265, 1995.

[24] Gawronski, W. "H_∞ controller for the DSS13 antenna with wind disturbance rejection properties," *TDA Progress Report,* vol.42-127, November 1996, tmo.jpl.nasa.gov/tmo/progress_report/42-127/127G.pdf

[25] U. Schoenhoff, A. Klein, and R. Nordmann, "Attitude control of the airborne telescope SOFIA: μ-synthesis for a large scaled flexible structure," *Proc. 39th IEEE Conf. Decision and Control*, Sydney, Australia, 2000.

[26] T. Erm, B.Bauvir, and Z. Hurak, "Time to go H-infinity?" *Proc. SPIE, Advanced Software, Control, and Communication Systems for Astronomy,* Glasgow, UK, vol. 5496, 2004.

[27] K. Li, E.B. Kosmatopoulos, P.A. Ioannou, and H. Ryaciotaki-Boussalis, "Large segmented telescopes: Centralized, decentralized and overlapping control designs," *IEEE Control Systems Magazine*, October 2000.

[28] K. Li, E.B. Kosmatopoulos, P.A. Ioannou, H. Boussalis, and A. Chassiakos, "Control techniques for a large segmented reflector," *Proc. 37th IEEE Conference on Decision and Control,* Tampa, FL, 1998.

[29] M. Whorton, G. Angeli, "Modern control for the secondary mirror of a Giant Segmented Mirror Telescope," *Proc. SPIE, Future Giant Telescopes*, vol.4840, 2003.

[30] Y. Peng, D. Vrancic, and R. Hanus, "Anti-windup, bumpless, and conditioned transfer techniques for PID controllers," *IEEE Control Systems Magazine,* vol.16, No.4, 1996.

[31] D. Mancini, M. Brescia, E. Cascote, P. Schipani, "A neural variable structure controller for telescopes pointing and tracking improvement," *Proc. SPIE,* vol.3112, 1997.

[32] Tyler, S. R., "A trajectory preprocessor for antenna pointing," *TDA Progress Repor*t, 42-118, pp. 139-159, 1994, tmo.jpl.nasa.gov/tmo/progress_report/42-118/118E.pdf

[33] J.J. Brandt, "Controlling the Green Bank Telescope," *Proc. SPIE, "Advanced Telescope and Instrumentation Control Software,* vol.4009, 2000.

[34] H. Baier, and G. Locatelli, "Active and passive microvibration control in telescope structures," *Proc. SPIE, Telescope Structures, Enclosures, Controls, Assembly/Integration/Validation and Commissioning,* vol. 4004, 2000.

[35] T.Erm, "Analysis of tracking performance," *Proc. SPIE, Optical Telescopes Of Today And Tomorrow*, vol.2871, p 1032-1040, 1996

[36] R. Kibrick, L. Robinson, V. Wallace, and D. Cowley "Tests of a precision tiltmeter system for measuring telescope position," *Proc. SPIE*, vol.3351, 1998.

[37] M. Cullum, and J. Spyromilio, "Thermal and wind control of the VLT," *Proc. SPIE, Telescope Structures, Enclosures, Controls, Assembly/Integration/Validation and Commissioning,*vol. 4004, 2000.

[38] W. Gawronski, F. Baher, and O. Quintero: "Azimuth track level compensation to reduce blind pointing errors of the Deep Space Network antennas," *IEEE Antennas and Propagation Magazine*, 2000, also tmo.jpl.nasa.gov/tmo/progress_report/42-139/139D.pdf .

[39] A. Greve, M. Dan, and J. Penalver, "Thermal behavior of millimeter wavelength radio telescopes," *IEEE Trans. on Antennas and Propagation*, vol.40, No.11, 1992.

[40] A. Greve, G. MacLeod, "Thermal model calculations of enclosures for millimeter wavelength radio telescopes," *Radio Science*, Vol.36, No.5, 2001.

[41] Gawronski, W., and Parvin, B., "Radiotelesope low rate tracking using dither," *AIAA Journal of Guidance, Control, and Dynamics*, vol.21, 1998.

[42] C. H. Rivetta, and S. Hansen, "Friction model of the 2.5 mts SDSS telescope," *Proc. SPIE*, vol.3351, 1998.

[43] A. Ramasubramanian, L.R. Ray, "Adaptive friction compensation using extended Kalman-Bucy filter friction estimation: a comparative study," *Proc. American Control Conf.*, Chicago, IL, 2000.

[44] J. Moreno, R. Kelly, and R. Campa, "On velocity control using friction compensation," *Proc 41st Conf. Decision and Control,* Las Vegas, NV, 2002.

[45] M. Feemster, P. Vedagarbha, D.M. Dawson, and D. Haste, "Adaptive control techniques for friction compensation," *Proc. American Control Conf.*, Philadelphia, PA, 1998.

[46] M. Nordin, and P.O. Gutman, "Controlling mechanical systems with backlash—a survey," *Automatica*, vol.38, pp.1633-1649, 2002.

[47] R. Dhaouadi, K. Kubo, and M. Tobise, "Analysis and compensation of speed drive system with torsional loads," *IEEE Trans. on Industry Applications*, vol.30, No.3, 1994.

[48] M.T. Mata-Jimenez, B. Brogliato, and A. Goswami "On the control of mechanical systems with dynamics backlash," *Proc 36th Conf. Decision and Control,* San Diego, CA, 1997.

[49] B. Friedland, "Feedback control of systems with parasitic effects," *Proc. American Control Conf.*, Albuquerque, NM, 1997.

[50] J.L. Stein, and C.-H. Wang, "Estimation of gear backlash: Theory and simulation," *Journal of Dynamic Systems, Measurement, and Control*, vol. 120, 1998.

[51] N. Sarkar, R.E. Ellis, and T.N. Moore, "Backlash detection in geared mechanisms: Modeling, simulation, and experimentation," *Mechanical Systems and Signal Processing*, vol.11, No.3, 1997.

[52] A.A. Stark, R.A. Chamberlin, J.G. Ingalis, J. Cheng, and G. Wright, "Optical and mechanical design of the Antarctic Submillimeter Telescope and Remote Observatory," *Rev. Sci. Instrumm* vol.68, 1997.

[53] W. Gawronski, J.J. Brandt, H.G. Ahlstrom, Jr., and E. Maneri: "Torque bias profile for improved tracking of the Deep Space Network antennas," *IEEE Antennas and Propagation Magazine*, Dec. 2000, also see tmo.jpl.nasa.gov/tmo/progress_report/42-139/139F.pdf

[54] W. Gawronski, and E. Craparo "Antenna scanning techniques for estimation of spacecraft position," *IEEE Antennas and Propagation Magazine*, vol.44, no.6, Dec. 2002, also see ipnpr.jpl.nasa.gov/tmo/progress_report/42-147/147B.pdf

[55] N. Levanon, "Upgrading conical scan with off-boresight measurements," *IEEE Trans. Aerospace and Electronic Systems*, vol.33, No.4, 1997.

[56] Gudim, M. A., W. Gawronski, W. J. Hurd, P. R. Brown, and D. M. Strain, "Design and performance of the monopulse pointing system of the DSN 34-meter beam-waveguide antennas," TMO PR 42-138, April-June 1999, pp. 1-29, August 15, 1999, tmo.jpl.nasa.gov/tmo/progress_report/42-138/138H.pdf

[57] Gawronski, W., and M.A. Gudim, "Design and performance of the monopulse control system," *IEEE Antennas and Propagation Magazine,* 1999, also see tmo.jpl.nasa.gov/tmo/progress_report/42-137/137A.pdf .